Influence of processing parameters on the fracture behaviour of 316L SS printed by laser powder bed fusion

T Wilson, M Sealy, I Cisa Bofarull, Clément Keller, B Vieille

To cite this version:

T Wilson, M Sealy, I Cisa Bofarull, Clément Keller, B Vieille. Influence of processing parameters on the fracture behaviour of 316L SS printed by laser powder bed fusion. Mechanics of Materials, 2024, 198, pp.105133. 10.1016/j.mechmat.2024.105133 . hal-04692205

HAL Id: hal-04692205
https://hal.science/hal-04692205v1

Submitted on 9 Sep 2024

Influence of processing parameters on the fracture behaviour of 316L SS printed by laser powder bed fusion

T. Wilson[1], M. Sealy[2], I. Cisa Bofarull[3], C. Keller[3], B. Vieille[4]

1 University of Nebraska-Lincoln, Mechanical and Materials Engineering, 1400 R Street, Lincoln, NE 68588, USA

2 Purdue University, School of Mechanical Engineering, 610 Purdue Mall, West Lafayette, IN 47907, USA

3 Laboratoire Génie de Production, Université de Tarbes Occitanie Pyrénées, Université de Toulouse, 47 Avenue d′Azereix, 65000 Tarbes, France

4 Normandie Univ, UNIROUEN, INSA Rouen, CNRS, Groupe de Physique des Matériaux, 76800 Saint-Étienne-du-Rouvray, France

Address correspondence to: benoit.vieille@insa-rouen.fr

This is a postprint version of the published version in Mechanics of Materials: https://doi.org/10.1016/j.mechmat.2024.105133. Thanks to Elsevier to publish this article.

Abstract

This study explored the relationship between process parameters and fracture behavior in 316L stainless steel printed by laser powder bed fusion. Fracture testing was conducted according to ASTM E1820 for single edge notch bending, and elastic mechanical properties were determined using ultrasonic surface wave analysis. Five test sets were considered in a vertical building configuration using five different volumetric energies belonging to conduction mode. The critical fracture toughness was calculated and discussed along with the plastic deformations at the crack tip. The study found that local plastic deformation for single edge notch bending was influenced by powder bed fusion process parameters. A correlation was observed between energy density, fracture toughness, and the dimensions of the fracture process zone. The R-curves showed different fracture behaviors depending on the energy density. The energy required to grow a crack was associated with larger plastic zones, resulting in fracture toughness values ranging from 43 (43 J.mm^{-3}) to 427 kJ/m² (68 J.mm^{-3}). Results are discussed in terms of porosity and strain hardening capacity depending on the manufacturing conditions.

Keywords: LPBF; process parameters; fracture behavior; ductility; toughness; ASTM E1820, 316L.

1. **Introduction**

Additive manufacturing (AM) is a promising process to manufacture parts with great geometrical intricacy, which cannot be manufactured by conventional processes. Among all AM processes, Laser Powder Bed Fusion (LPBF) is nowadays employed industrially in different sectors such as automotive, aeronautics, biomedicine…for titanium, aluminum, nickel, iron-based alloys [1-10]. Due to the out-of-equilibrium character of the process involving cooling rates of about 10^6 K.s^{-1}, the microstructure generated by the process widely differs from those obtained for conventional processes. Alloys manufactured by LPBF generally exhibit porosity (lack-of-fusion or keyholes), crystallographic and morphologic textures, dendritic structures associated with dislocation cells as well as precipitation. These microstructural characteristics can be partially controlled by the usual process parameters such as laser power and speed, layer-to-layer disorientation, hatch distance or layer thickness leading to a wide range of potential mechanical properties [4-20]. For the correct design of the industrial parts, it is of prime importance to correctly understand the relationship between the process parameters, the microstructure and the mechanical properties of the alloys.

When it comes to mechanical properties in tension or fatigue, the great effort paid by the mechanics of material community in the last decades enabled a correct understanding of this relationship. In tension for instance, there is a great consensus on the fact that LPBF alloys exhibit generally better mechanical properties (higher yield stress and higher elongation) compared to conventional wrought/cast alloys. Those tensile properties depend on the orientation of tensile direction with respect to the building direction due to crystallographic and morphologic grain structure generated by the process [3-4][6-7][11-12][15-16]. Moreover, it has been proved that the processing parameters strongly affect the microstructure and mechanical properties through the volumetric energy applied on the material. Larger volumetric energies tend to generate stronger texture, larger grain and dendrite sizes leading to lower yield stresses [11-12,19]. Low volumetric energies may also lead to the formation of lack-of-fusion, which have a detrimental effect on the ductility of the material [7-8]. In fatigue, many works agreed about the strong dependence of the fatigue life on manufacturing defects such as porosity (mainly lack-of-fusion), surface roughness and surface residual stresses. These three features tend to decrease the fatigue life [13-14, 20] regardless of the alloy family leading the sample post-operational treatments (machining, polishing, heat-treatment, high isostatic pressure…) to mitigate this effect [3-7, 15-18].

As far as fracture toughness is concerned, there are less references dealing with the understanding of the link between the LPBF induced microstructure and this property [21-29]. Fracture toughness deserves, nevertheless, special attention in particular in industrial sectors such as the energy production one. Similarly to fatigue, the porosity was reported to be detrimental to fracture toughness as pores can interact with the crack propagation and may represent a preferential path in case of large porosity ratio [24-27]. It was also reported that precipitation associated with the dendritic solidification is detrimental to fracture toughness [24], which can be affected by heat treatments. Due to the layer-by-layer construction of the material as well as the elongated grains formation depending on the LPBF parameters, the fracture toughness is also dependent on the crack orientation with respect to the lasing planes [21-22, 24]. As reported for nickel-based superalloys, a crack propagating parallel to the lasing planes leads to significantly larger fracture toughness than a crack propagating perpendicular to the lasing planes [21-22]. Nevertheless, to the best author's knowledge, only a few works has been devoted to the characterization of the influence of the manufacturing parameters on fracture toughness, in particular the influence of the volumetric energy applied during the manufacturing, which can vary from a manufacturer to another and may induce fracture behavior.

The objective of this study is to estimate the fracture toughness of 316L stainless steel printed by laser powder bed fusion. 316L is employed due to its wide industrial interest in energy production as well as its almost monophasic character which simplify the understanding on the relationship between the fracture toughness and microstructure. Five different volumetric energies belonging to conduction mode and close to the lack-of-fusion regime were considered due to their industrial interest associated to lower mechanical properties' anisotropy [14-15] as well as lower building times [15]. Those different energies are obtained modifying the laser power and speed in the process. Fracture testing was based on the American Society for Testing and Materials (ASTM) standard E1820 for single edge notch bending (SENB) [30]. By means of microscopic observations and surface profilometry, porosity and the dimensions of the plastic zone were assessed and then correlated with energy density and fracture toughness. Results show a particular dependence on porosity and strain hardening rate leading to the existence of a maxima for the fracture toughness.

2. Materials and Methods

2.1 Laser powder bed fusion (LPBF)

The specimens for SENB tests were printed by LPBF on an EOS M290 SI2649 by the Volum-e company (France). The powder was 316L stainless steel with an average powder particle diameter of about 34 µm. Twenty-five total specimens were printed as vertically oriented rectangular columns (Figure 1a) based on the dimensional limits expressed in ASTM E1820 [30].

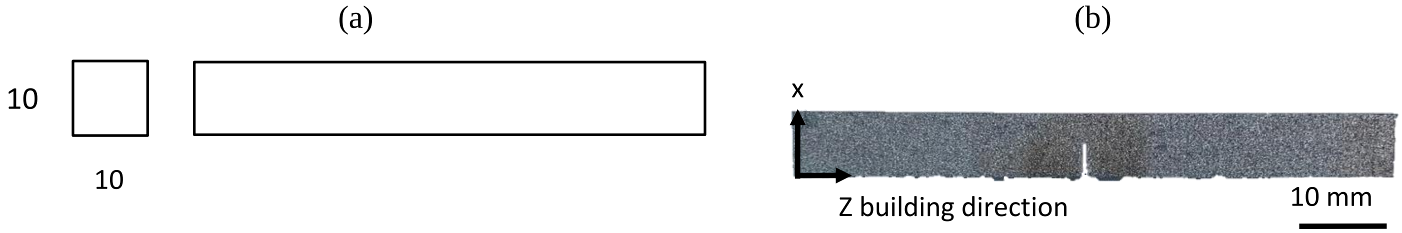

Figure 1 – Single Edge Notched Bending specimens' geometry: (a) Sample dimensions used for testing. All dimensions are in mm and (b) SENB specimens after notching.

Five different manufacturing conditions were applied (5 samples per condition). The standard printing parameters are summarized in Table 1. Those conditions were optimized to obtain high density and equiaxed microstructure reducing the potential anisotropic mechanical behavior [16]. The theoretical energy density (E_v) is provided in Table 2 and calculated using Eqn. 1:

$$E_v = \frac{P}{vht} \quad (1)$$

where P is the laser power (J/s), v is the scanning speed (mm/s), h is the hatch spacing (mm), and t is the layer thickness (mm). For the standard printing parameters, the volumetric energy is about 54 J.mm^{-3}. The other four manufacturing conditions were chosen to simulate fluctuation (±20%) in terms of laser power and speed around the standard configuration. These fluctuations can be linked, for instance, to fumes or calibration deviation of the LPBF machine and are also representative of the general variation in these parameters in literature.

For each condition, only one parameter (i.e. laser power or speed) is modified by a factor of 20% with respect to the standard conditions. Table 2 summarizes the lasing conditions for each set of manufacturing parameters. As only one parameter is modified, each modified lasing condition is explained by the affected parameter (laser power: P or laser speed: L) and the amount of modification. All manufacturing conditions are labeled from A to E, A being the standard one and B, C, D and E the modified ones. Following literature, all these conditions belong to conduction mode in the limit with the lack-of-fusion domain [17-18]. All those volumetric energies are expected to generate equiaxed microstructure without pronounced columnar grains and crystallographic texture, which is generally targeted by industries.

After printing, specimens were removed from the build plate and notched by wire electrical discharge machining (EDM). The wire diameter was 0.3 mm. The notch was cut in the center of the column to a nominal depth of 5 mm (Figure 1b).

Table 1– LPBF build parameters

Parameter		Value
Laser power	P	195 W
Scan speed	v	900 mm/s
Layer thickness	t	40 μm
Hatch spacing	h	0.1 mm
Hatch orientation		67˚

Table 2 – Theoretical volumetric energy in J/mm^3

AM Parameters		E_v
Standard (A)		54.2
Velocity high (B)	V + 20%	45.1
Velocity low (C)	V - 20%	65.0
Power high (D)	P + 20%	67.7
Power low (E)	P - 20%	43.3

No heat treatment was applied after processing making all the specimens “as built” as close as possible to the industrial case. Moreover, as reported in literature, heat-treatment will modify the size and spatial distribution of nano-oxide which can mask the effect of the volumetric energy on mechanical properties.

2.2 Sample density and porosity analyses

From the five aforementioned different lasing conditions, a modification of the density of the lased material is expected. Hence, the relative densities were then measured with an Archimedes type balance (with 0.1g accuracy) using a reference theoretical value of 8 g/cm^3. For each sample, an average of five measurements was performed in order to consider the experimental scattering. To have more insight regarding the amount and size of pores induced by the process, digital image analysis coupled with an optical microscope was carried out on sample planes either perpendicular or parallel to the building direction. To this aim, cross sections of virgin samples were cutted and submitted to conventional metallographic preparation (polishing SiC paper from 800 to 4000 followed by diamond paste polishing and final ultra-sonic cleaning). The microscope magnification was set up to 100x ensuring a pixel size of about 0.06 µm. Series of 5 images were acquired at random places in the two kinds of cross sections for the five manufacturing conditions and then submitted to a thresholding procedure enabling the characterization of the porosities by ImageJ software.

2.3 Mechanical properties assessment

The estimation of the critical strain energy release by the ASTM E1820 standard requires the mechanical properties of the material both in the elastic and plastic domains. In order to quantify the fracture toughness as accurately as possible, the elastic modulus as well as the yield stress and ultimate tensile strength for each manufacturing configuration must be considered. When it comes to the elastic properties, a MISTRAS Eurosonic ultrasonic scanner (module UTC 100 RF) was used for finding the longitudinal Young’s modulus and Poisson’s ratio [33]. Measurements were taken at the top and bottom of each specimen parallel to the expected crack propagation direction. The signal was monitored by means of the software EuroscanV. Prior to testing, the wave speed software was setup and measurements were taken for each specimen. The plastic mechanical properties were estimated using conventional tensile tests. Flat tensile samples with a gauge section of 20x10x1 mm following the standard ISO6892-1:2019 [34] were first extracted by EDM from 20x20x100 mm blocks manufactured with the same conditions as the SENB samples. 3 samples per manufacturing conditions were then submitted to displacement control tensile loading ensuring an average strain rate of about 0.001 /s.

2.5 Surface analyses

The surface profilometry of the 316L SS specimens were measured to compare the amount of out of plane plastic deformation at the crack tip and the wedge positions (Figure 2). Surface scans were performed on a Keyence VHX-1000 optical digital microscope and profiles were measured at the crack tip and the region of maximum deformation caused by the wedge. The wedge position would cause the bulging outward of material as the compressive load was increased. The fracture process zone would cause the material around the crack to recede under the tensile forces.

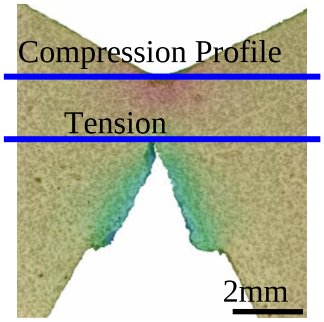

Figure 2 – The locations of the surface scans where the deformation profile was measured by means of a 3D numerical optical microscope for each specimen.

2.6 Fracture toughness

ASTM E1820 outlines the process to prepare the test, and to calculate the fracture toughness of ductile materials. The preparation of the specimen involves meeting specific geometric and surface roughness requirements. When it comes to the mechanical testing, the ASTM standard reports a displacement control mode. Nevertheless, a preliminary testing campaign strictly following this standard leads to some issues regarding the measurement of the crack extension and the associated fracture toughness of AM 316L. Consequently, the following deviations from this standard were necessary: (i) no precracking of the specimen, (ii) stress control testing condition, and (iii) crack propagation estimation by digital image analysis. Indeed, EDM notches are sufficiently narrow to provide the sharp crack tip that localizes the stress concentration and reduces the plane stress region on the surface avoiding a long step of fatigue pre-cracking. Displacement control on AM specimens causes multiple crack tips to propagate concurrently which makes difficult the understanding of the role played by the AM microstructure over the crack propagation. Load control testing of the specimens reduced the amount that a secondary tip would form and extend and consequently applied in our case [21-22]. Digital image analysis allowed for the direct measurement of the crack growth while disregarding the plastic blunting effects prior to crack initiation and extension.

The specimen geometry was determined by the following relationships between the span (*S*), width (*W*), and thickness (*B*) (Figure 3). The span is the distance between the center of the rollers. The ratio for the span and width is defined as:

$$S = 4W \tag{2}$$

and the width to thickness ratio for a specimen is defined as:

$$S = 4W \tag{3}$$

The maximum surface roughness (R_a) was required to be less than 63 µm for edge planes and 125 µm for side planes far above the one measured for our samples (about 15 µm). The edge planes are the surfaces in contact with the rollers and the wedge applying the force. The squareness of applicable parallel and perpendicular planes needs to be within 0.5˚.

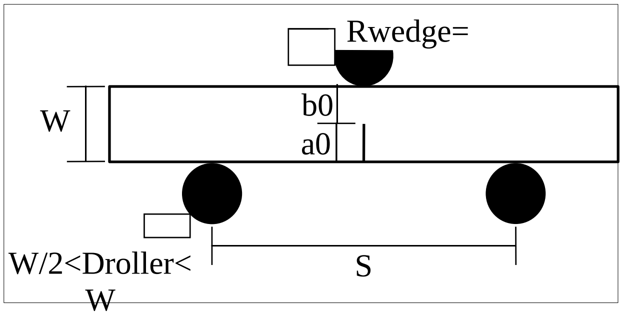

Figure 3 – Single Edge Notched Bending specimen and test alignment geometry requirements following ASTM E1820 standard.

The applied load to use is the mean force (P_m) and is calculated by the following equation:

$$P_m = \frac{0.5 B b_0^2 \sigma_Y}{S} \tag{4}$$

where b_0 is the original remaining ligament and σ_Y is the effective yield strength whose value is calculated by the equation:

$$\sigma_Y = \frac{\sigma_{YS,0.2} + \sigma_{TS}}{2} \tag{5}$$

where $\sigma_{YS,0.2}$ is the yield strength at a 0.2% plastic strain offset, and σ_{TS} is the ultimate tensile strength of the material to be tested. In the present case, those mechanical properties were evaluated for each manufacturing conditions by tensile tests as specified in section 2.3.

According to the ASTM standard E1820, the resulting data from the SENB test is used to determine the resistance or J-R curve. A fracture toughness (J_i) value is calculated at each point for a given crack length (a_i), displacement (v_i), and force (P_i). The fracture toughness is the sum of the elastic fracture toughness (J_{el}) and the plastic fracture toughness (J_{pl}) at a given point in time. The elastic fracture toughness is based on a stress intensity factor and elastic mechanical properties. The plastic fracture toughness is based on the geometry of the specimen, the crack propagation, and the area under the force displacement curve after being corrected for elastic compliance:

$$J_i = J_{el,i} + J_{pl,i}$$

(6)

$J_{el,i}$ is calculated by the equation:

$$J_{el,i} = \frac{K_i^2(1-\nu^2)}{E}$$

(7)

where K_i is the stress intensity factor at the specific time, and E and v are the Young's Modulus and Poisson's Ratio respectively for the tested material. The stress intensity factor is calculated by the following equation for a specimen without side grooves:

$$K_i = \left(\frac{P_i S}{BW^{3/2}}\right) f\left(\frac{a_i}{W}\right)$$

(8)

where

$$f\left(\frac{a_i}{W}\right) = \frac{3\left(\frac{a_i}{W}\right)^{1/2}\left[1.99 - \frac{a_i}{W}\left(1-\frac{a_i}{W}\right)\left(2.15 - 3.93\frac{a_i}{W} + 2.7\left(\frac{a_i}{W}\right)^2\right)\right]}{2\left(1+2\frac{a_i}{W}\right)\left(1-\frac{a_i}{W}\right)^{3/2}}$$

(9)

for a load-line displacement test, $J_{pl,I}$ is calculated by the equation:

$$J_{pl,i} = \left[J_{pl(i-1)} + \frac{1.9}{b_{i-1}}\left(\frac{A_{pl,i} - A_{pl(i-1)}}{B}\right)\right]\left[1 - 0.9\left(\frac{a_i - a_{i-1}}{b_{i-1}}\right)\right]$$

(10)

where $A_{pl,i}$ is the plastic area relating to the force and displacement at the specified time. It is calculated by the equation:

$$A_{pl,i} = A_{pl(i-1)} + \frac{(P_i + P_{i-1})\left(v_{pl,i} - v_{pl(i-1)}\right)}{2}$$

(11)

where $v_{pl,i}$ is the plastic component of the load line displacement at the specified time. It is calculated by the equation:

$$v_{pl,i} = v_i - (P_i C_i)$$

(12)

where C_i is the compliance of the material. When the compliance is not found experimentally, it is necessary to use the following equation under load-line testing for a specimen without side grooves:

$$C_i = \frac{1}{EB}\left(\frac{S}{W - a_i}\right)^2 \left[1.193 - 1.98\frac{a_i}{W} + 4.478\left(\frac{a_i}{W}\right)^2 - 4.443\left(\frac{a_i}{W}\right)^3 + 1.739\left(\frac{a_i}{W}\right)^4\right]$$

(13)

The critical fracture toughness (J_{Ic}) for mode I is the intersection of the power law regression line that corresponds to the experimental data and the linear line based on the strength of the material and the change in crack extension (Figure 4a). A minimum and maximum offset limit run parallel to the linear fracture toughness formula. Any values that fall outside the offset limits are supposed to be ignored in the calculation of the power law. The value for J_{max} is supposed to be below the limit. The linear fracture toughness line is determined by:

$$J = 2\sigma_Y \Delta a$$

(14)

(a) (b)

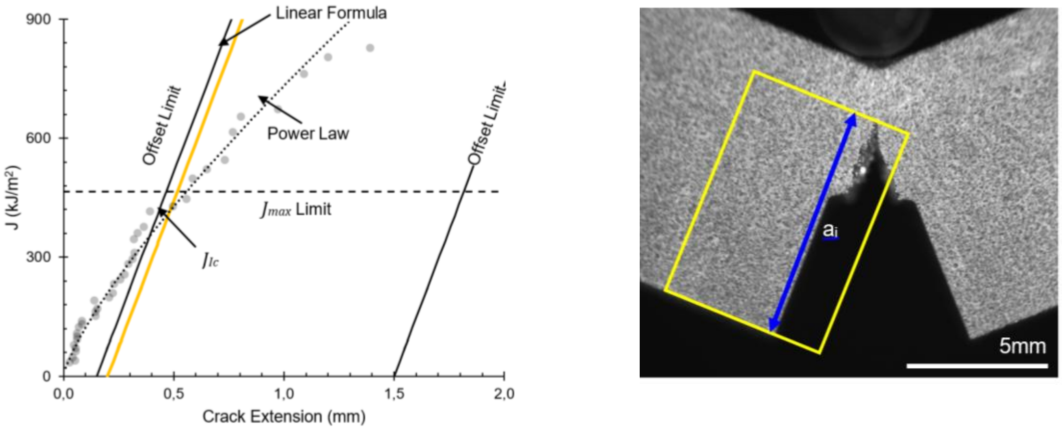

Figure 4 – (a) Graphical view of the limits and zones for which valid data points are to be included in calculating the J_{Ic} as outlined in ASTM E1820 and (b) Measurement of crack extension from a digital image sequence.

The crack extension was measured using ImageJ software. The initial image was used to set the scale for the image sequence. The crack extension values were measured in each image perpendicular from the base surface to the crack tip (Figure 4b). The image sequence being analyzed started at the end of material blunting when the initial crack appeared up to the end of the crack propagation. The yellow rectangle was moved and rotated with respect to the bottom edge of the specimen and then resized to line up with the crack tip.

Ductile materials are characterized by a ductile tearing once the crack is initiated. To get a better understanding of the resistance to crack propagation, it is therefore relevant to quantify the crack propagation by computing the tearing modulus T [31], defined as follows in agreement with the ASTM standard E1820:

$$T = \frac{E}{{\sigma_{YS}}^2}\frac{dJ}{da}$$

(15)

Where E is the Young Modulus and σ_{YS} is the yield stress determined from monotonous tensile tests.

According to ASTM E1820, the Irwin's requirement should be met to validate the value of fracture toughness. It stipulates that the size of the plastic zone depends on the applied stress, the mechanical properties of the material, and the size of the crack. The higher the applied stress, the larger the plastic zone, and the more likely the crack will propagate. In addition, crack propagation occurs when the elastic strain energy stored in the material is equal to the energy required to create a new crack surface. This occurs when the size of the plastic zone reaches a critical size called the critical crack length r_p. The size of this plastic zone r_p around the crack tip in the case of mode I loading and plane-strain state can be calculated as follows [32]:

$$r_p = \frac{1}{3\pi}\left(\frac{K_{Ic}}{\sigma_y}\right)^2 \tag{16}$$

2.7 Single edge notch bending test

Fracture tests were conducted on an MTS 810 hydraulic testing machine equipped with a 100 kN load cell under load control (Figure 5). The rate was 50 N/s with a maximum displacement limit of 10 mm. The specimen was placed on the three-point bending platform with the span set to 40 mm. The loading wedge had a radius of approximately 1 mm. All specimens were preloaded at 200 N to prevent vibrational movement while setting up the remainder of the test equipment.

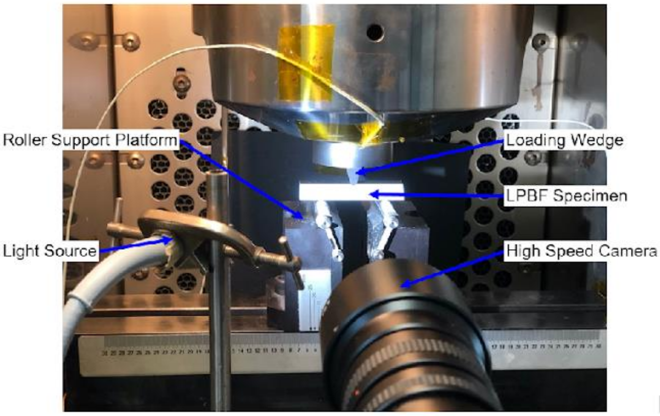

Figure 5 – Single edge notched bending test setup: the high-speed camera allows an in-situ measurement of crack extension from a digital image sequence during fracture testing

Digital image analysis allowed for direct comparison between the crack growth and applied load. Images of the SENB test were recorded by a Grasshopper3 high-speed monochrome camera. The camera was set up to collect images every 50 ms on average using Vic-Snap 8 camera software. This allowed for a direct comparison between the individual load cell values and measured crack growth. To increase the contrast and to reduce the reflectivity, each specimen was airbrushed with a thin coat of white acrylic polyurethane and additional lighting was used to brighten the surface during the test. ImageJ (Version 1.53) was used for post-processing to accurately measure the crack growth in each image sequence.

3. Results and Discussion

3.1 Mechanical properties

The wave speed and density measurements were used to calculate the average elastic properties for each specimen configuration (Table 3). All specimen configurations were compared to the available data of wrought 316L SS (UNS S31603) [35]. The values for the elastic properties were all calculated and found to be lower than wrought 316L SS. While lower, they are within the expected range depending on the heat treatment and post-processing of wrought 316L stainless steels.

The densities of the AM specimens all resulted in lower values compared to wrought 316L SS, probably due to some variations in the chemical composition between wrought reference and the employed 316L powder as well as to manufacturing defects such as lack-of-fusion. When comparing between the different configurations, there is a direct correlation between the energy density and the material density. The lower volumetric energies would most likely have an increased proportion of lack of fusion leading to lower densities [27]. In order to accurately assess the presence of manufacturing defects which can lower the density and can act as local stress risers affecting the crack propagation, Table 4 summarizes the density estimated using digital image analysis using the procedure mentioned above. All specimens are characterized by a very low porosity ratio, between 0.07 to 0.87%, depending on the manufacturing conditions and observation plane. Even if those values agree with those generally reported for high-density samples, the average value obtained from horizontal and vertical planes depends linearly on the volumetric energy applied for the manufacturing.

Table 3 – Elastic properties (measured by ultrasound) as a function of the density energy

Configuration	Energy Density (J/mm^3)	Poisson's Ratio	Young's Modulus (GPa)	Shear Modulus (GPa)
UNS S31603*	n/a	0.3	200	82
A (standard)	54.2	0.262±0.003	200±1.6	79.3±0.7

B (V+20%)	45.1	0.289±0.002	187±1.1	72.7±0.5
C (V -20%)	67.7	0.283±0.004	191±1.1	74.3±0.6
D (P +20%)	65.0	0.285±0.003	192±0.8	74.6±0.4
E (P -20%)	43.3	0.269±0.002	191±1.3	75.1±0.5

*Properties from ATI 316L Austenitic Stainless-Steel Datasheet for comparison [35]; +- values indicate the standard deviation

Table 4 – Porosities analyses of 316L SS specimens printed by LPBF

Configuration	Volumetric mass (kg/m^3)	Relative density (%)	Horizontal plane (%)	Vertical plane (%)	Average (%)
A (standard)	7987±23	99.6±0.4	99.48	99.94	99.71
B (V+20%)	7936±18	99.2±0.3	99.13	99.88	99.51
C (V -20%)	7910±38	98.9±0.5	99.77	99.93	99.85
D (P +20%)	7956±09	99.4±0.2	99.74	99.84	99.79
E (P -20%)	7944±15	99.3±0.2	99.59	99.36	99.48
Average value	7949±33	99.4±0.4	99.54±0.3	99.79±0.2	99.66±0.2

In order to correctly compute the fracture toughness values according to equations (13-14) and the tearing modulus based on equation (15), the yield stress and ultimate tensile strength of each manufacturing condition must be evaluated. Figure 6a shows the macroscopic tensile responses for each configuration, from which the tensile properties are calculated (Figure 6b). There is no clear trend on the evolution of the tensile properties as a function of the volumetric energy density with an average yield stress of about 490 MPa and an ultimate tensile strength of about 780 MPa. Moreover, it clearly appears that the tensile behaviour is elastic ductile with a constant strain hardening.

(a) (b)

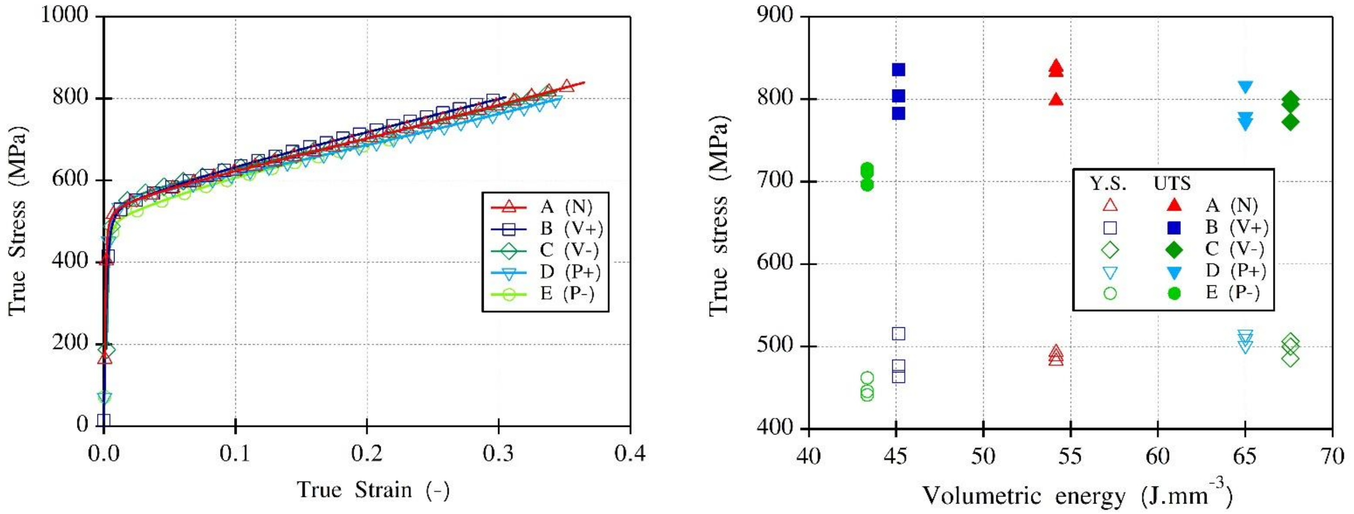

Figure 6 – Influence of process parameters on the tensile behaviour of 316L SS printed by LBPF: (a) stress-strain curves – (b) Changes in the Ultimate tensile Strength (UTS) and the plastic yield strength (Y.S.) as a function of the volumetric energy density.

3.2 Fracture behavior testing

As reported previously in vertically Hastelloy X LPBF built specimens, displacement control of the bending test associated with the layering in LPBF processes leads to multiple crack tips formation, preventing an accurate calculation of fracture toughness [22]. Indeed, at the crack initiation, two crack tips would appear. As the specimen continued under displacement control, both crack tips would propagate in a mostly even manner. Load control was hence performed to have a constant force rate that would cause a higher stress concentration on the dominant crack as it formed. Under load control, the presence and propagation of multiple crack tips was still present, but the crack growth of the secondary crack was reduced and the crack path would follow mainly the dominant crack (see Appendix). All SENB results discussed herein happened under load control at a rate of 50 N/s to a maximum displacement of 10 mm as specified in the previous section. The SENB test resulted in showing the difference in ductility and crack stability for each configuration (Figure 7a). The standard (A), P +20% (D) and V-20% (C) configurations required a higher force before crack initiation and resulted in a ductile material with stable crack growth. These configurations had higher energy densities. For V +20% (B) and P -20% (E), the specimens were less ductile and resulted in unstable crack growth and a reduced force for crack initiation.

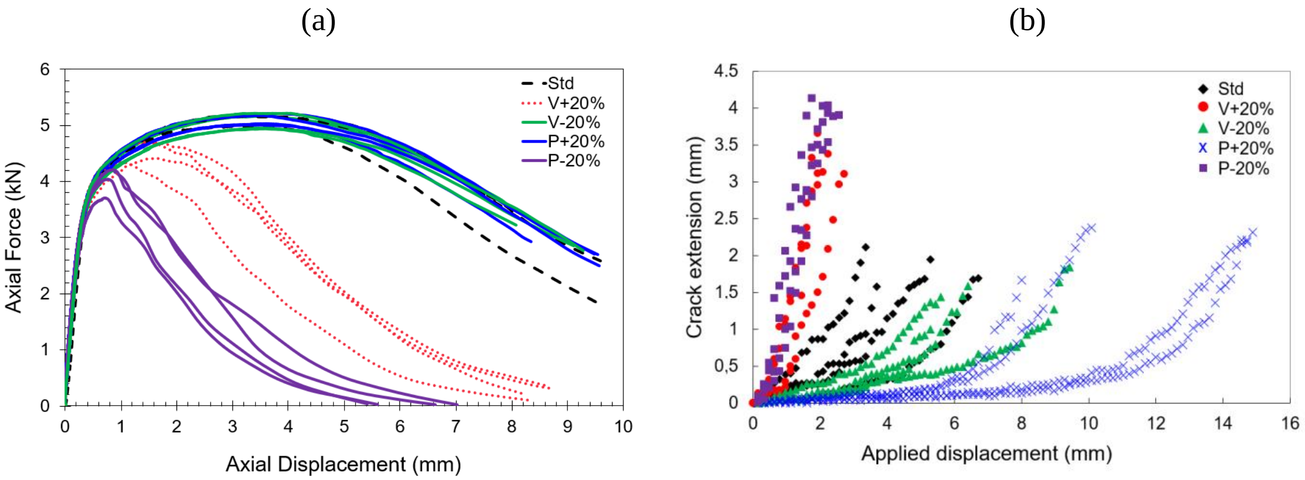

Figure 7 – Macroscopic bending responses depending on the process parameters: (a) force-displacement curves for all test specimens and (b) evolution of crack extension as a function of time (from crack initiation)

The lowest forces and fastest crack growth were seen in P -20% specimens (E), which were also the lowest energy density (99.48%). Figure 7b shows the influence of process parameters on the crack extension rate. With respect to the standard configuration, it appears that the crack extension is slowed down for higher energy densities (P+20% - D and V-20% - C) whereas it is accelerated at lower energy densities. These results suggest that the fracture mechanisms, characterized by the crack extension rate and total crack length, are driven by process parameters, which are associated with specific microstructures. One also expects this difference to reflect on the values of the fracture toughness at initiation.

3.3 Fracture toughness calculations

According to ASTM standard E1820 described in section 2.2, the calculated values for the 316L SS specimens reveal a varied fracture toughness based on the configuration parameters (Figure 8). Each graphed dataset shows the crack extension limits, J_{max} limit, linear fracture toughness line, and the best-fit power law curve (Table 5). The intersection of the linear fracture toughness and the power law is the critical fracture toughness value. This value is expected to be below the J_{max} limit. ASTM E1820 is designed for calculating the fracture toughness in welds and wrought metals.

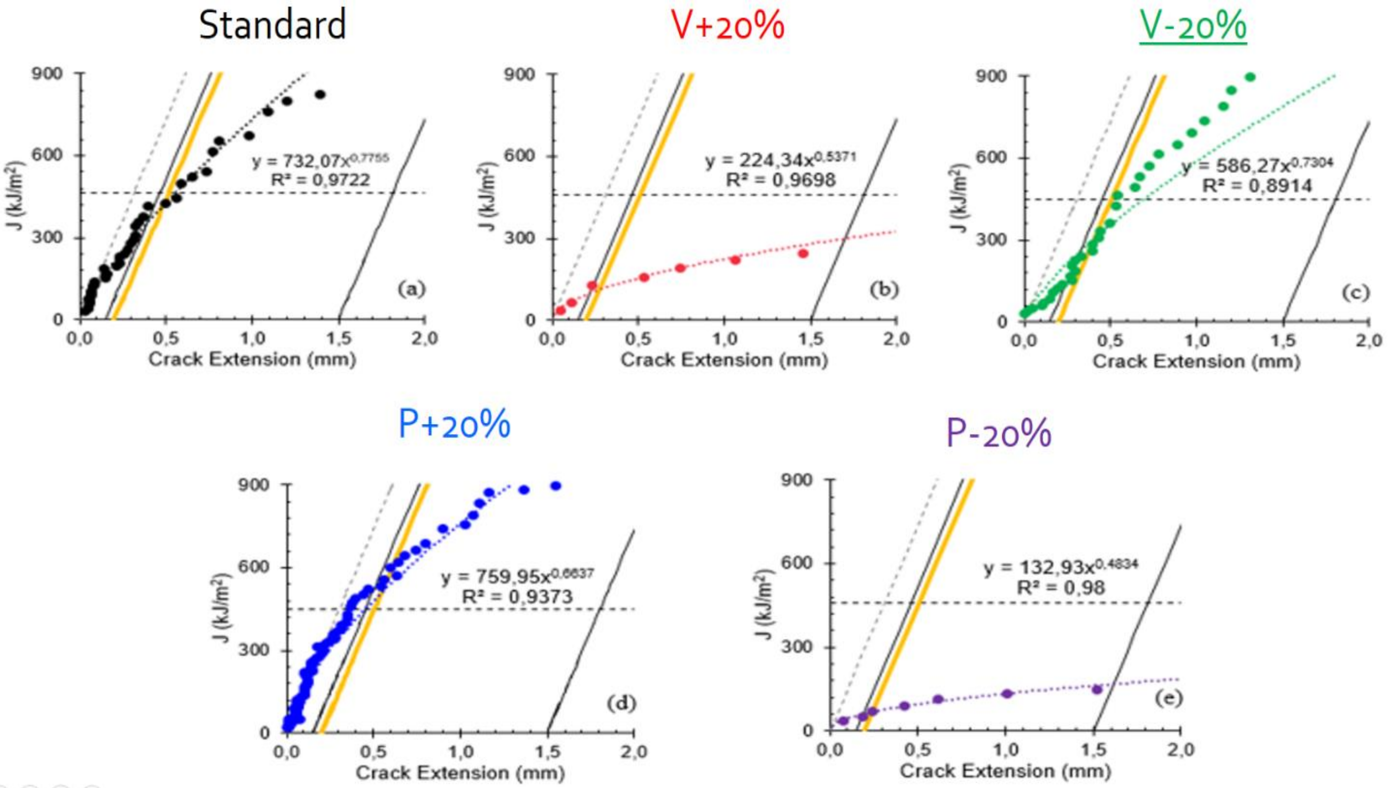

Figure 8 – The graphs representing the fracture toughness values from the crack extension for the (a) A - standard, (b) B - V +20%, (c) C - V-20%, (d) D - P+20%, and (e) E - P-20% configurations. The linear fracture toughness line (orange) and power law (dotted) show the intersection representing the critical fracture toughness value.

The fracture response for the more ductile specimens (standard - A, V -20% - C, and P +20% - D) showed the need for larger fracture energies to extend the crack. As the crack propagated, these configurations were able to dissipate part of the energy in material deformation. To continue the crack propagation, higher amounts of energy had to be applied. The power law for these configurations resulted in a response more closely resembling a linear increase in as the crack was extended. The crack extension in the less ductile configurations (V +20% - B and P -20% - E) saw a different response in fracture toughness values. In these configurations, as the crack propagated, the fracture toughness values quickly leveled off. The material was not able to dissipate much of the applied load into material deformation. The power law in these two configurations both reached an asymptotic response characterizing the unstable crack propagation.

Table 5 – Averaged power law and resulting critical toughness

Configuration	Power Law	J_{Ic} (kJ/m^2)
Standard	$J = 568.9\Delta a^{0.8966}$	235.9±109.2
V +20%	$J = 241.2\Delta a^{0.6120}$	109.3±53.5
V -20%	$J = 660.9\Delta a^{0.7759}$	347.0±75.1
P +20%	$J = 686.3\Delta a^{0.6669}$	426.6±58.4
P -20%	$J = 85.2\Delta a^{0.4666}$	42.8±15.9

3.4 Correlation between local plastic deformation and crack propagation

In metals characterized by ductile fracture, the plastic zone at the crack point is a critical region for the measurement of material toughness, as it represents the ability of the material to absorb energy before fracture. If the plastic zone is too small, the material sample may fail before it has absorbed enough energy to provide an accurate measure of toughness. Alternatively, if the plastic area is too large, the material sample may absorb too much energy, which may mask differences in toughness between different materials. Plastic deformation plays, hence, a key role in the propagation of a crack in a ductile material. Local plasticity prevents crack initiation by redistributing stresses around the crack tip, therefore reducing the stress concentration. Once a crack propagates, new surfaces are created from the release of elastic energy stored in the material. The plastic deformation dissipates the energy released by the crack propagation, which ultimately slows down the crack propagation.

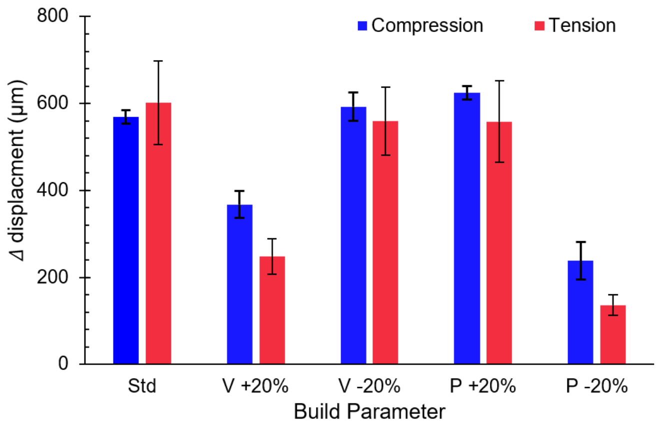

Figure 9 – Comparison between the compressive and tensile displacements for the build configurations. The load wedge location is related to the compressive displacement and the crack tip is associated with the tensile displacement (the error bars are computed from the data dispersion shown in Figure 8)

Each specimen had a surface profilometry scan done to measure the amount of out of plane displacement at the wedge and crack tip (Figure 9). On the one hand, as observed in Figure 10(a) and Figure 10(b), this displacement is limited to a surface length extending approximately ± 2.5 mm from the peak, whatever the analyzed sample. The effects of the loading wedge on the plastic behavior of the material were limited to that region. On the other hand, the results of the scans follow a similar trend as the load-displacement curve generated from the SENB tests (Figure 7).

Indeed, Figure 9 and Figure 10 reveal that the configurations that had high ductile behavior (A, C, D) and stable crack propagation also had the highest out of plane deformation about 600 µm. This shows that the increase in energy density had no effect on the amount of out of plane deformation that the specimens would undergo when loaded. The measured displacement for these three-sample series is also similar in the compressive and tensile zones. These figures also suggest that the two tested samples manufactured using the lower energy density (B, E) behaved differently, both in total magnitude and the profile stress state. When the energy density was lowered, the magnitude of the displacement was also lower by a factor 2 or 3. A difference between the compressive and tensile profile stress state also appeared in Figure 9 and Figure 10. The lower amount of deformation at the crack tip reveals the material to have a reduced local plasticity compared to the higher energy densities.

During mechanical loading, a portion of the mechanical energy brought to the specimen is dissipated (as heat) in the plastic zone at the crack tip, where plastic deformation occurs. This initial phase corresponds to the blunting at the crack tip before crack initiation. These plastic deformations can also help slow down crack propagation by redistributing stresses around the crack tip and absorbing the energy released by crack propagation, hence reducing the rate of crack propagation as observed in Figure 7b.

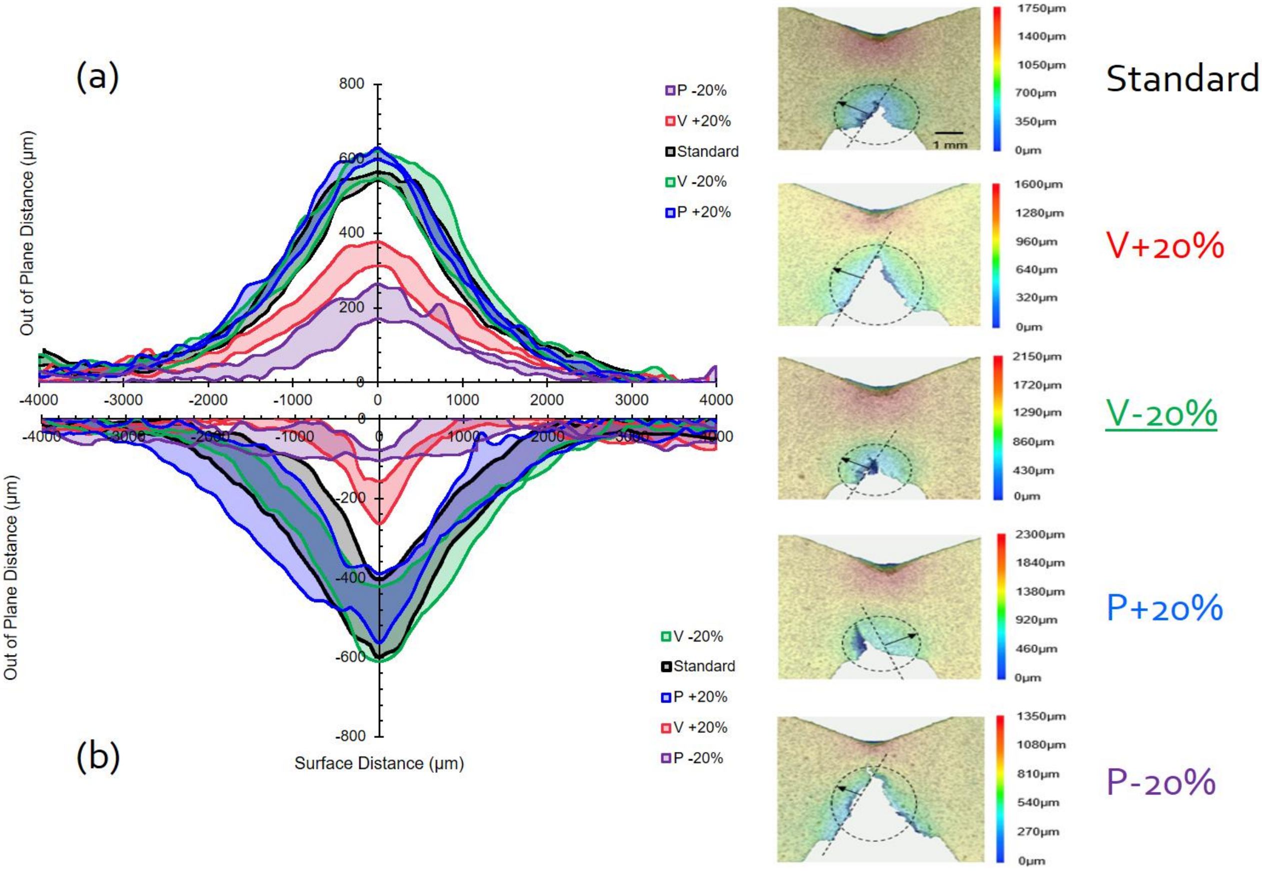

Figure 10 – Outer surface profilometry – The isovalues fields on the right-hand side show the out of plane displacement due to the (a) compressive forces of the loading wedge and (b) tensile forces caused by the crack tip opening. Circles represent the Fracture Process Zone in tension and the arrows provide a rough estimate of the width of the plastic zone

3.5 Correlation between fracture behavior and volumetric energy density

Based on results of table 5, Figure 11 shows that the changes in the fracture toughness J_{Ic} as well as the tearing modulus of 316L SS specimens manufactured by LPBF as a function of the volumetric energy density Ev. Ductile materials as 316L SS specimens printed by LPBF are characterized by a ductile tearing once the crack is initiated, the tearing modulus T values were computed from equation (15) and the power laws identified from the J-R curves shown in Figure 9. The evolution of the two parameters exhibits a particular trend with a maximal value obtained for Ev ranging between 57 and 63 J.mm^{-3}. The decreasing evolution in the fracture toughness observed on the black dotted curve is confirmed by considering the value drawn from [24] in the case of 316L SS specimens (Compact Tension geometry) manufactured by LBPF. To further compare the fracture toughness values to the ones obtained in the literature, wrought 316L SS specimens (SENB geometry) are characterized by a fracture toughness $J_{Ic} = 290\,\frac{kJ}{m}^2$ that is within the range of values obtained from LPBF specimens [23]. The tearing modulus value $T = 500$ computed for wrought 316L SS specimens also belongs to the range of fracture toughness values computed for LPBF specimens.

To model the evolution of fracture toughness and tearing modulus of 316L SS elaborated by LPBF as a function of the volumetric energy, a log-normal regression law whose parameters are given in Table 6 can be employed:

$$J_{Ic}(Ev) = J_0 + \alpha . e^{\left\{-\left[\frac{ln\left(\frac{Ev}{Ev0}\right)}{\beta}\right]^2\right\}} \tag{17}$$

Table 6 – Parameters of a log normal regression law to predict the fracture toughness J_{Ic} of 316L SS specimens printed by LPBF as a function of the volumetric energy density Ev

J_0 (kJ/m^2)	α	$Ev0$ $(J/mm^3$	β
76.08	381.93	62.21	0.15

Table 4 reports that the higher the volumetric energy, the lower the sample porosity. This feature can explain the increasing dependency of the fracture toughness and tearing modulus on the volumetric energy on the left-hand side part of figure 11 but cannot be responsible for the decreasing trend observed for higher volumetric energies. As explained earlier, plastic deformation at crack tip can help to absorb the energy released by crack propagation. This energy absorption reduces the rate of crack propagation, and modify, in turn, the fracture mechanisms. Figure 6(a), representing the tensile curves of the different sample series, illustrates similar hardening for all manufacturing conditions followed by slight differences in strain hardening rate between the sample series [36]. The analysis of the derivative of the tensile curves in the linear domain enables the estimation of the strain hardening rate which is plotted as a function of the volumetric energy in figure 12.

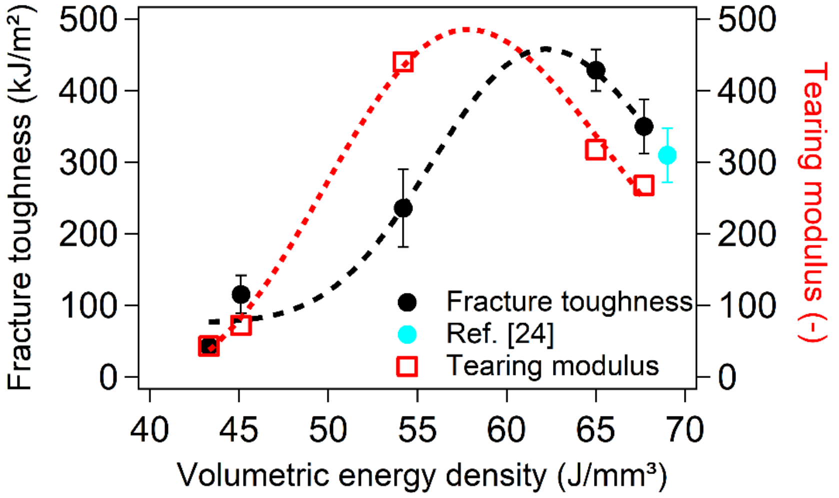

Figure 11 – Changes in the fracture toughness and tearing modulus in 316L SS printed by LPBF as a function of volumetric energy density. Reference [24] was considered here to confirm the decreasing trend in fracture toughness as Ev increases.

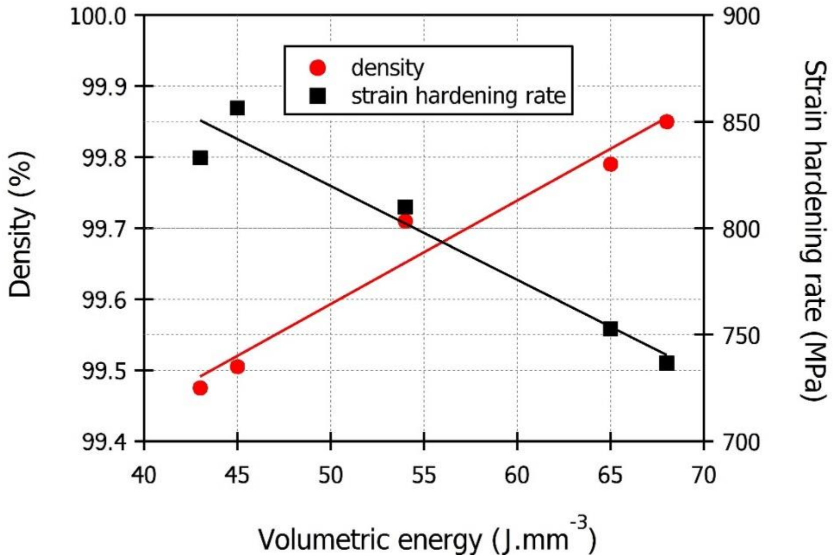

Figure 12 – Evolution of the density and strain hardening rate as a function of the volumetric energy applied for LPBF manufacturing.

Contrarily to the density, also plotted in this figure, the strain hardening rate decreases almost linearly with the applied volumetric energy. The evolution of the two curves of figure 12 suggests the existence of optimized volumetric energy leading to a compromise between density and strain hardening rate which fits well with the one related to maximum value of fracture toughness and tearing modulus (see figure 11). Consequently, both porosity and strain hardening ratio seem to be involved in the fracture toughness and tearing modulus with the volumetric energy. For low values of Ev, porosity drives the fracture mechanisms with a very high sensitivity on this parameter. In that case, the porosity network is expected to strongly interact with the crack propagation (preferential path), significantly reducing the amount of plastic deformation at the crack tip (characterized by the out-of-plane displacement on figure 10). For larger values of *Ev*, fracture mechanisms are dominated by the strain hardening ratio. Indeed, the very low porosity is expected not to affect the crack propagation which is controlled by the plastic deformation at crack tip. As the strain hardening ratio decreases with the volumetric energy, the energy absorbed during the crack propagation is also reduced with *Ev*. Thus, the fracture toughness and tearing modulus also diminish with the increase in volumetric energy as observed in figure 12. An extended microstructure and mechanical characterization at lower scale must be performed to confirm this mechanism.

4. Conclusions

In this paper, the fracture toughness of 316L manufactured by LPBF using varied laser power and scanning speeds (in the range of conduction mode) in the vertical orientation was estimated using ASTME1820 standard. Bending tests of single edge notched samples were performed as well as porosity/density measurement followed by mechanical properties in tension. Based on the analysis of the bending curves, the material properties, the out-of-plane displacement at fracture and the estimation of the fracture toughness, the following conclusions can be drawn.

First, the process parameters significantly affect the ductility and fracture behavior in AM specimens printed by LPBF. Estimated fracture toughness and tearing modulus are in the order of magnitude of those reported for wrought cast 316L. Second, the energy required to grow a crack is associated with larger plastic zones resulting in fracture toughness values ranging from 43 to 427 kJ/m² depending on the manufacturing conditions. Fracture stability and J_{Ic} values were seen in the higher energy density specimens. Unstable fracturing and significantly reduced J_{Ic} values were seen in the lower energy densities. In addition, sample porosity and strain hardening capacity seem to control both fracture toughness and tearing modulus with the existence of a maximal value. Finally, the fracture toughness and tearing modulus are extremely sensitive to the volumetric energy due to porosity for low values of *Ev*.

An extended microstructure and mechanical characterization of the different samples need to be performed to understand the origin of the relationship between lasing energy and fracture toughness.

Data availability statement

The data that support the findings of this study are available from the corresponding author upon reasonable request.

References

[1] H. Gaja, F. Liou. Defects monitoring of laser metal deposition using acoustic emission sensor. The International Journal of Advanced Manufacturing Technology 2017 ; 90(1-4) : 561-574. Doi: 10.1007/s00170-016-9366-x

[2] G. Ziolkowski, E. Chlebus, P. Szymczyk, J. Kurzac. Application of X-ray CT method for discontinuity and porosity detection in 316L stainless steel parts produced with SLM technology. Archives of civil and mechanical engineering 2014; 14 : 608-614. Doi: 10.1016/j.acme.2014.02.003

[3] M.S.I.N. Kamariah, W.S.W. Harun, N.Z. Khalil, F. Ahmad, M.H. Ismail, S. Sharif. Effect of heat treatment on mechanical properties and microstructure of selective laser melting 316L stainless steel. Materials Science and Engineering 2017 ; 257 :12-21. Doi: 10.1016/j.msea.2019.01.110

[4] K. Li, D. Li, D. Liu, G. Pei, L. Sun. Microstructure evolution and mechanical properties of multiple-layer laser cladding coating of 308L stainless steel. Applied Surface Science 2015 ; 340 : 143-150. Doi: 10.1016/j.apsusc.2015.02.171

[5] L.N. Carter, C. Martin, P. J. Withers, M.M. Attallah. The influence of the laser scan strategy on grain structure and cracking behaviour in SLM powder-bed fabricated nickel superalloy. Journal of Alloys and Compounds 2014 ; 615 : 338-347. Doi: 10.1016/j.jallcom.2014.06.172

[6] T. Bhardwaj, M. Shukla. Effect of laser scanning strategies on texture, physical and mechanical properties of laser sintered maraging steel. Materials Science and Engineering : A 2018 ; 734 : 102-109. Doi: 10.1016/j.msea.2018.07.089

[7] D. Dai, D. Gu, H. Zhang, J. Xiong, C. Ma, C. Hong, R. Poprawe. Influence of scan strategy and molten pool configuration on microstructures and tensile properties of selective laser melting additive manufactured aluminum-based parts. Optics Laser Technology 2018 ; 99 : 91-100. Doi: 10.1016/j.optlastec.2017.08.015

[8] F. Geiger, K. Kunze, T. Etter. Tailoring the texture of IN738LC processed by selective laser melting (SLM) by specific scanning strategies. Materials Science and Engineering : A 2016 ; 661 : 240-246. Doi: 10.1016/j.msea.2016.03.036

[9] E. Yasa, J. Deckers, J-P Kruth. The investigation of the influence of laser remelting on density, surface quality and microstructure of selective laser melting parts. Rapid Prototyping Journal 2011; 17(5) : 312-327. Doi: 10.1108/13552541111156450

[10] Lewandowski, J. J., and Seifi, M. Metal Additive Manufacturing: A Review of Mechanical Properties. Annual Review of Materials Research 2016, 46(1) pp. 151-186. Doi: 10.1146/annurev-matsci-070115-032024

[11] Margerit, P., Weisz-Patrault, D., Ravi-Chandar, K. Tensile and ductile fracture properties of as-printed 316L stainless steel thin walls obtained by directed energy deposition. Additive Manufacturing 2021; 37: 101664. Doi: 10.1016/j.addma.2020.101664.

[12] C. Keller, M. Mokhtari, B. Vieille, H. Briatta, P. Bernard. Influence of a rescanning strategy with different laser powers on the microstructure and mechanical properties of Hastelloy X elaborated by powder bed fusion. Materials Science and Engineering: A 2021; 803: 140474. Doi: 10.1016/j.msea.2020.140474

[13] Riemer, A., Leuders, S., Thöne, M., 2014, "On the Fatigue Crack Growth Behavior in 316L Stainless Steel Manufactured by Selective Laser Melting," Engineering Fracture Mechanics, 120pp. 15-25. Doi: 10.1016/j.engfracmech.2014.03.008

[14] Charmi, A., Falkenberg, R., Ávila, L., Mohr, G., Sommer, K., Ulbricht, A., Evans, A. Mechanical anisotropy of additively manufactured stainless steel 316L: An experimental and numerical study. Materials Science and Engineering: A 2021, 799, 140154. Doi: 10.1016/j.msea.2020.140154

[15] Leicht, A., Rashidi, M., Klement, U., Hryha, E. Effect of process parameters on the microstructure, tensile strength and productivity of 316L parts produced by laser powder bed fusion. Materials Characterization 2020, 159, 110016. Doi: 10.1016/j.matchar.2019.110016

[16] Nguejio, J., Mokhtari, M., Paccou, E., Baustert, E., Khalij, L., Hug, E., Bauster E., Bernard P., Boileau S., Keller, C. Combined effect of a spread powder particle size distribution, surface machining and stress-relief heat treatment on microstructure, tensile and fatigue properties of 316L steel manufactured by laser powder bed fusion. The International Journal of Advanced Manufacturing Technology 2023, 1-21. Doi: 10.1007/s00170-023-11008-w

[17] Diaz Vallejo, N.; Lucas, C.; Ayers, N.; Graydon, K.; Hyer, H.; Sohn, Y. Process Optimization and Microstructure Analysis to Understand Laser Powder Bed Fusion of 316L Stainless Steel. Metals 2021, 11, 832. Doi: 10.3390/met11050832

[18] Ziri, S., Hor, A., Mabru, C. Combined effect of powder properties and process parameters on the density of 316L stainless steel obtained by laser powder bed fusion. The International Journal of Advanced Manufacturing Technology 2022, 120(9-10), 6187-6204. Doi: 10.1007/s00170-022-09160-w

[19] S.S. Joshi, C. Keller, E. Hug, W. Lefebvre. Quantifying microstructural contribution to yield stress and strain hardening of Ni20Cr alloy manufactured by laser powder bed fusion with different volumetric energy densities. Journal of Alloys and Compounds 2023, 968: 172241, Doi: 10.1016/j.jallcom.2023.172241.

[20] A. Avanzini. Fatigue Behavior of Additively Manufactured Stainless Steel 316L. Materials 2023; 16(1):65. Doi: 10.3390/ma16010065

[21] Vieille, B., Keller, C., Mokhtari, M., 2020, "Investigations on the Fracture Behavior of Inconel 718 Superalloys obtained from Cast and Additive Manufacturing Processes," Materials Science and Engineering: A, 790pp. 139666. Doi: 10.1016/j.msea.2020.139666

[22] B. Vieille, A. Duchaussoy, S. Benmabrouk, R. Henry, C. Keller. Fracture behavior of Hastelloy X elaborated by laser powder bed fusion: Influence of microstructure and building direction. Journal of Alloys and Compounds 2022; 918:165570. Doi: 10.1016/j.jallcom.2022.165570

[23] Picker, C. The fracture toughness of Type 316 steel and weld metal. International Working Group on Fast Reactors; p. 915-937; Chester (UK); 10-14 Oct 1983.

[24] E. de Sonis, S. Dépinoy, P-F. Giroux, H. Maskrot, P. Wident, O. Hercher, F. Villaret, A-F. Gourgues-Lorenzon. Microstructure – Toughness relationships in 316L stainless steel produced by laser powder bed fusion. Materials Science and Engineering: A 2023; 877: 145179. Doi: 10.1016/j.msea.2023.145179

[25] C.M. Davies, O. Withnell, T. Ronnerberg, R. Williams, P. Hooper. Fracture analysis of 316L steel samples manufactured by Selective Laser Melting. Procedia Strucural Integrity 2018; 13 : 1384-1389. Doi: 10.1016/j.prostr.2018.12.289

[26] E.E. Tan, F.S. Sorce, C.M. Davies. Fracture Toughness Testing of 316L Steel Manufactured by Laser Powder Bed Fusion. In proceedings of ASME 2022 Pressure Vessels & Piping Conference, July 17–22, 2022, Las Vegas, Nevada, USA.

[27] Pitrmuc Z, Šimota J, Beránek L, Mikeš P, Andronov V, Sommer J, Holešovský F. Mechanical and Microstructural Anisotropy of Laser Powder Bed Fusion 316L Stainless Steel. Materials. 2022; 15(2):551. Doi: 10.3390/ma15020551

[28] Conway, K. M., Kunka, C., White, B. C. Increasing Fracture Toughness Via Architected Porosity. Materials & Design 2021; 205: 109696. Doi: 10.1016/j.matdes.2021.109696

[29] Kumar, D., Jhavar, S., Arya, A., 2021, "Mechanisms Controlling Fracture Toughness of Additively Manufactured Stainless Steel 316L," International Journal of Fracture, pp. 1-18. Doi: 10.1007/s10704-021-00574-3

[30] ASTM, 2022, "Test Method for Measurement of Fracture Toughness - ASTM E1820.

[31] El Khatib, O., Hütter, G., Pham, RD. et al. A non-iterative parameter identification procedure for the non-local Gurson–Tvergaard–Needleman model based on standardized experiments. Int J Fract 241, 73–94 (2023). Doi: 10.1007/s10704-023-00689-9

[32] G.R. Irwin. Analysis of stresses and strains near the end of cracking traversing a plate. J. Appl. Mech. 24, 361 (1957). Doi: 10.1115/1.4011547

[33] ASTM, 2022, "Standard Terminology for Nondestructive Examinations - ASTM E1316.

[34] Test standard ISO6892-1:2019. Metallic materials — Tensile testing — Part 1: Method of test at room temperature

[35] ATI, "ATI 316L™ Austenitic Stainless-Steel Technical Data Sheet," 2022.

[36] S.S. Joshi, C. Keller, L. Mas, W. Lefebvre, E. Hug, J-P. Couzinié. On the origin of the strain hardening mechanisms of Ni20Cr alloy manufactured by laser powder bed fusion. International Journal of Plasticity 2023, 165: 103610. Doi: 10.1016/j.ijplas.2023.103610